Full Paper

Interpreting Experimental Results from Shock Impacts on Single Crystal PETN in the Context of Continuum Models

Darby J. Luscher,*[a] Marc J. Cawkwell,[a] Kyle J. Ramos,[a] Richard L. Sandberg,[a] and Cynthia A. Bolme[a]

Abstract: In this paper we interpret previous experimental measurements of impacts on single crystal PETN in the context of a simple continuum model. Hugoniot calculations using the simple model framework under various limiting assumptions envelope measured Hugoniot states reasonably well and suggest that non-negligible deviatoric elastic strains may exist in the shock compressed state for weak impacts. An accompanying simple kinematic model for lattice deformation was used to estimate the expected shifts in X-ray diffraction peaks for the (211) plane under impacts normal to (110) planes. The results suggest that negligible relaxation of the deviatoric lattice deformation occurs on the short (10–20 ns) time and wave propagation (40–80 m) scales of laser-driven shock experiments, and that the corresponding elastic strains may be large. Because of the potentially large deviatoric elastic strains, the specific finite deformation strain measure used within thermomechanical single crystal models is of significant consequence, which is explored numerically by the comparison of isothermal purely elastic responses under uniaxial and simple shear deformations.

Keywords: PETN · anisotropy · single crystal · continuum model · impact

1 Introduction

Defects and microstructural features at the mesoscale have a profound effect on the shock sensitivity of solid explosives [1, 2]. The collapse of voids of sub-micron dimensions is crucial for the initiation and stable propagation of a detonation. We are able to control the shock sensitivity of explosives, albeit empirically, by controlling the defect content of the explosive grains and through processing steps that reduce the severity of stress concentrators [3–7].

The ability to simulate how explosive materials and plastic bonded composites interact with shock waves at the mesoscale to generate hot spots would allow us to develop improved or tailored explosives *in silico*. This ambitious goal requires high fidelity models for the thermomechanical response of the constituent materials over the relevant strain rates and length and time scales. Those spatial and temporal scales are far beyond the reach of any all-atom molecular dynamics simulation for the foreseeable future. Hence, continuum-scale representations of the constituents are essential.

Explosive molecular crystals tend to be brittle and highly anisotropic. While explosives are qualitatively very different from metallic materials, whose thermomechanical properties are well understood, their underlying deformation mechanisms are similar and encompass dislocation mediated plasticity, deformation twinning, and cleavage fracture [8–10]. While the details may differ significantly, we can approach the development of thermomechanical models for molecular materials in the same way we would any other crystalline solid.

Continuum models can be informed by simulations at lower length scales using density functional theory or molecular dynamics simulations. However, these simulations are mainly useful for obtaining those properties that do not depend on strain rate. These include equation of state [11], elastic constants [12], thermal expansion coefficients [13], driving forces for phase transformations [14], surface energies, and may potentially help identify deformation mechanisms. On the other hand, the behavior of the constituents under dynamic conditions must still be determined from carefully designed experiments [15–19].

We shall describe the many challenges in using the information obtained from common shock physics experiments to build, parameterize, and validate continuum scale models for energetic constituents, with a particular focus on the elastic-plastic behavior of pentaerythritol tetranitrate (PETN) at high rates. Interface velocimetry measurements from gas gun-driven flyer plate experiments are an indirect probe of the underlying anisotropic thermomechanical response of the material. Nevertheless, when these measurements can be interpreted within the framework of a physics-based materials model, we can develop a true mechanistic picture of the thermomechanics at high rate.

[a] *D. J. Luscher, M. J. Cawkwell, K. J. Ramos, R. L. Sandberg, C. A. Bolme*
Los Alamos National Laboratory
Los Alamos, New Mexico 87545
USA
*e-mail: djl@lanl.gov

In situ X-ray imaging and diffraction experiments at national user facilities allow us to move beyond indirect measurements of the deformation and phase behavior of crystalline materials. Nevertheless, the interpretation of data from *in situ* experiments is not trivial. Hence, thermomechanical models are useful for both designing and understanding complex *in situ* experiments, plus those experiments can be used to parameterize and validate the same models.

The crystal structure of PETN is simple in comparison to many energetic molecular crystals [20]. It adopts a primitive tetragonal unit cell containing only two molecules. Nevertheless, it displays strong plastic anisotropies despite its relatively high symmetry. It has a relatively high impact sensitivity and exhibits a unique inflection in its Pop-plot, which has led to its use in the study of shock and impact initiation.

In the following sections, we outline simple yet powerful models that can be used to understand and interpret traditional wave-speed measurements and *in situ* X-ray diffraction data in PETN. These models allow us to evaluate the degree to which inelastic relaxation of deviatoric stresses occurs during shock experiments. We subsequently demonstrate and discuss the importance of using the appropriate strain measures in materials, like molecular crystals, that can undergo large elastic deformations.

2 Summary of Previous Experiments

Halleck and Wackerle conducted dynamic experiments to measure the elastic precursor behavior in single-crystal PETN with impacts on (110) and (001) orientations over shock stresses ranging from 0.6 to 4.0 GPa and specimen thicknesses ranging approximately 3–5 mm [21]. They measured incident and transmitted stress time histories using a quartz flyer impacting the PETN specimen, which was backed by another quartz window. The quartz acted as a piezoelectric gauge from which the stress-strain histories were obtained. The wave speeds associated with the elastic precursor were calculated directly using the difference in the time of arrival of the stress waves and the known specimen thickness. The particle velocity of the elastic precursor was inferred from analytical impedance matching solutions using the measured stress state and specimen/gauge interface velocity. Halleck and Wackerle used a dislocation-density based continuum theory to interpret the observed elastic precursor decay and to explain the apparent increase in the Hugoniot elastic limit with increasing shock strength [21].

Dick and Ritchie [22] investigated the orientation dependence of impact sensitivity in single crystal PETN using gas gun-driven flyer plate impact experiments. In their experiments, oriented single crystal specimens approximately 3–6 mm in thickness were located between quartz anvil and PMMA window. The entire target configurations were impacted by an aluminum flyer plate at various impact velocities. The interface velocity time histories between PETN specimen and PMMA window were measured using VISAR. Dick [23] performed similar experiments as those previously performed by Dick and Ritchie, but especially focused on (110) impacts at shock pressures of 3–12 GPa within the PETN in order to characterize the unusual inflection in the Pop-plot of PETN for that particular orientation.

Bolme et al. have conducted laser-driven shock experiments on PETN at the Linac Coherent Light Source (LCLS) facility located at the Stanford Linear Accelerator Center (SLAC) [24]. *In situ* measurements of the dynamic material response were obtained using an X-ray free electron laser (XFEL) and appropriate detectors to collect data for coherent diffraction imaging (CDI) and X-ray diffraction (XRD) analysis of the deformed lattice. Their investigation was focused on the collapse of 10 μm voids within single crystal PETN, the mechanistic details of which is outside of the focus of the present study; however, their efforts at characterizing the laser-drive conditions along with the measured diffracted intensity satisfying the Bragg condition enable an estimate of the shock compressed state of the lattice, and importantly, an assessment of the magnitude of elastic strains attainable over short time periods and weak shock conditions.

2.1 Dislocation-mediated Plasticity in PETN

Dislocation-mediated plasticity in PETN has been studied heavily owing to its proposed role in controlling the anisotropic impact sensitivity of PETN. Only one slip system, which involves dislocations with Burgers vector (111) gliding on the {110} planes, has been identified unambiguously from experiment and simulations [25–26]. Recent density functional theory calculations have provided some insight into why dislocations with such a long Burgers vector are seen in PETN at all, and why slip has not been seen on the {101} planes [27].

The limited number of slip systems in PETN gives rise to a strong plastic anisotropy. The sensitivity of oriented PETN single crystal to shock compression mirrors the plastic anisotropy whereby orientations with a small Hugoniot elastic limit are relatively insensitive whereas those orientations with a high Hugoniot elastic limit are sensitive.

The {110}(111) slip system is active for those orientations with a low Hugoniot elastic limit. However, interface velocimetry measurements alone cannot tell us which slip systems might be active for impacts on orientations with a high Hugoniot elastic limit. Several groups have proposed additional slip systems or deformation mechanisms that might be activated under shock conditions [22, 28–30]. Furthermore, X-ray topographic studies have identified dislocations with Burgers vectors other than (111), but whether these dislocations are glissile and on which planes they might glide is currently unknown [31]. Additional shock experiments, both traditional plate impact experiments and

with *in situ* imaging and diffraction will be required to identify those additional deformation mechanisms.

3 Theory and Modeling

The intention of this investigation is to relate observations from several different experiments in the context of a simple continuum representation of the dynamic material response. For this purpose, we use an anisotropic description of PETN thermoelasticity combined with simple approximations pertaining to the inelastic deformation. The deformation of the material is described by the deformation gradient, $\mathbf{F}$, which is multiplicatively decomposed into two parts,

$$\mathbf{F} = \mathbf{F}_e \mathbf{F}_{in} \tag{1.1}$$

where $\mathbf{F}_e$ represents the lattice deformation, and $\mathbf{F}_{in}$ the cumulative effects of inelastic mechanisms within the material and is assumed to have no effect on the lattice strain. We use the so-called Euler measure of elastic lattice strain defined as $\boldsymbol{\varepsilon} = \frac{1}{2}(\mathbf{I} - \mathbf{F}_e^{-1}\mathbf{F}_e^{-T})$ [32]. The Helmholtz free energy is assumed to take the form (cf. [16])

$$\rho_0\psi = \rho_0\psi_{eos}(V, T) + \frac{1}{2}\boldsymbol{\varepsilon} : \mathbb{C}(P) : \boldsymbol{\varepsilon} - \frac{1}{2}K(P)\varepsilon_V^2 \tag{1.2}$$

where ψ_{eos} is the Helmholtz free energy (per unit mass) associated with the volumetric response and is defined by the equation of state developed for PETN by Cawkwell *et al.* [11] and is the effective volumetric strain. Accordingly, the conjugate stress within the intermediate configuration is $\boldsymbol{\Sigma} = \rho_0\partial\psi/\partial\boldsymbol{\varepsilon}$ and the corresponding Cauchy stress is obtained by the elastic push-forward of the covariant coefficients, i.e. $\boldsymbol{\sigma} = J_e^{-1}\mathbf{F}_e^{-T}\boldsymbol{\Sigma}\mathbf{F}_e^{-1}$, where $J_e = \det \mathbf{F}_e$ [32].

3.1 Simple Model for Hugoniot Calculations

The simplified model for evaluating experimental observations of Hugoniot wave speed versus particle velocity measurements is based on solutions of the Rankine-Hugoniot jump equations, i.e.,

$$e_2 = e_1 + \frac{1}{2}(|\sigma_{11,2}| + |\sigma_{11,1}|)(V_1 - V_2) \tag{1.3}$$

which relates the internal energy per unit mass, e_k, the component of stress normal to the wave front, and the specific volume per unit mass. The subscripts '1' and '2' refer to points ahead of and behind the wave discontinuity, respectively. Solutions of Equation (1.3) for various cases are developed by identifying the appropriate initial stress, specific volume, and specific internal energy, and by defining the appropriate closure relations for that case. Our approach follows the general methodology of Udaykumar *et al.* [33] and Lieberman *et al.* [34] extended for anisotropic

thermoelasticity and our choice of the Euler finite-deformation elastic strain measure.

3.1.1 Solutions for Cases with a Single Wave

Single wave solutions pertaining to the cases of i) purely elastic loading, ii) purely hydrostatic loading, and iii) overdriven elastic-inelastic response, in which there is no leading elastic precursor wave will be considered. The difference between each of these cases is the closure relationship between the axial component of stress and the specific volume and specific internal energy. In all single wave cases the axial stress is computed by

$$\sigma_{11} = \sigma'_{11} - P_{eos}(\lambda V_0, T) \tag{1.4}$$

and the specific internal energy is computed according to

$$e = \psi_{EoS}(\lambda V_0, T) - T\frac{\partial\psi_{EoS}}{\partial T} + \psi' \tag{1.5}$$

The particular relationships used for the deviatoric contributions to free-energy, ψ', and axial stress, σ'_{11}, are outlined below for each single wave case. The solution strategy is to initialize $e_1 = e_0, V_1 = V_0$, and $\sigma_{11,1} = 0$. Then, for each value of λ set $V_2 = \lambda V_0$ and solve Equation (1.3) for T_2, e_2, and $\sigma_{11,2}$ using Equations (1.4) and (1.5) as closure. Finally, the shock wave velocity is computed as

$$U_s = \left(\frac{V_0|\sigma_{11,2}|}{1 - \lambda}\right)^{1/2} \tag{1.6}$$

and the particle velocity as

$$u_p = (1 - \lambda)U_s \tag{1.7}$$

Purely thermoelastic loading: While purely elastic loading is unlikely, there is a range of measurements over which the elastic-precursor wave (which is governed by these expressions) is dominant and the inelastic behavior is negligible.

Under a purely elastic response, the deviatoric stress is approximated as

$$\sigma'_{11} = (1 - \lambda^{-2})\left(\frac{\mathbb{C}_{11}}{3\lambda^3} - \frac{\mathbb{C}_{12} + \mathbb{C}_{13}}{6\lambda}\right) \tag{1.8}$$

where the elastic lattice coefficients are computed at the value of pressure obtained from the equation of state. The lattice elastic coefficients measured by Sun *et al.* [35] are used here, for reason explained in Ref. [12], and are transformed into a coordinate basis corresponding to uniaxial loading with the specified (*hkl*) planes aligned in parallel along the global 'X_1'-direction.

Purely hydrostatic loading: The case of purely hydrostatic loading, i.e. zero deviatoric stress, is consistent with solid materials that can easily accommodate any imposed deviatoric deformation via inelastic mechanisms that are inviscid with zero resistance. In some sense, this corresponds to a perfectly plastic flow that occurs at zero deviatoric stress. Numerically, this case is a lower bound for the shock velocity at any given particle velocity and is representative of the limiting behavior of shock response as shock pressures increase. The solution strategy involves using solely the equation of state to capture the nonlinear hydrostatic thermoelasticity, i.e. $\sigma'_{11} = 0$ and $\psi' = 0$.

Single overdriven elastic-inelastic wave: In this case, the Hugoniot state is presumed to be at some final non-zero deviatoric stress and energy, which is proportional to the elastic limit stress state. Consider an idealized elastic limit (i.e. yield state) that can be defined either by an equivalent yield stress, Y, or the critical value of shear stress on a particular (anisotropic) slip system to drive substantial dislocation motion, τ^α_Y. The corresponding value of λ_Y under conditions of uniaxial compressive strain can be identified directly from the constitutive equations (1.8) subject to the elastic limit conditions

$$Y = \left(\tfrac{3}{2}\boldsymbol{\sigma}' : \boldsymbol{\sigma}'\right)^{1/2} \tag{1.9}$$

or

$$\tau^\alpha_Y = \mathbf{s}^\alpha \cdot \boldsymbol{\sigma}' \cdot \mathbf{n}^\alpha \tag{1.10}$$

where $\mathbf{n}^\alpha$ and $\mathbf{s}^\alpha$ are the slip system normal convector and slip direction, respectively, for a crystallographic slip system, α. Using either of these approaches, one can identify the elastic limit state as $(\lambda_Y, \sigma'_{11,Y}, \psi'_Y)$. We assume that the deviatoric stress at the limit state may be relaxed or hardened through the inelastic process, such that the deviatoric stress and energy at the final Hugoniot state are $\sigma'_{11,2} = \eta\,\sigma'_{11,Y}$ and $\psi'_2 = \eta^2\psi'_Y$, respectively, where η is a relaxation (i.e. $0 < \eta < 1$) or hardening coefficient (i.e. $\eta > 1$). For complete relaxation of the deviatoric stress through inelastic mechanisms, $\eta = 0$, and this case reduces to the purely hydrostatic solution.

3.1.2 Solutions for Cases with an Elastic Precursor Followed by Second Wave to Final Hugoniot State

For cases with an elastic precursor wave that is travelling faster than the secondary shock wave to the final Hugoniot state, the solution scheme must account for two jumps, namely from initial ambient conditions to the Hugoniot elastic limit (HEL) state and subsequently from the HEL state to the final Hugoniot state. This scenario was solved quasi-analytically by Udaykumar *et al.* [33] for isotropic hypoelastic perfectly plastic deformation, and generalized to hyperelastic perfectly plastic deformation by Lieberman

et al. [34]. Here we adapt these solutions for the case of anisotropic thermoelasticity employing an Eulerian elastic strain measure in an approximate manner.

The approach begins with identification of the axial compression, $\lambda_{HEL} = \lambda_Y$, using either Equation (1.9) or (1.10). Next, Equation (1.3) is solved for the case where '1' corresponds to the initial ambient state, i.e. $e_1 = e_0, V_1 = V_0$, and $\sigma_{11,1} = 0$ and '2' corresponds to the HEL state behind the pre-cursor wave, i.e. $V_2 = \lambda_{HEL}V_0$, where the same closure relations and solution strategy as in the purely elastic case is used to identify T_{HEL}, e_{HEL}, and $\sigma_{11,HEL}$. From the solution $\sigma_{11,2} = \sigma_{11,HEL}$, Equations (1.6) and (1.7) are used to compute the elastic precursor wave velocity, U_e, and particle velocity, $u_{p,e}$, respectively.

The second step in the solution comprises solving Equation (1.3) for the case where '1' corresponds to the HEL state, i.e. $e_1 = e_{HEL}, V_1 = \lambda_{HEL}V_0$, and $\sigma_{11,1} = \sigma_{11,HEL}$ and '2' corresponds to the final Hugoniot state behind the secondary wave, to compute $\sigma_{11,2}$. Similar to the overdriven elastic-inelastic case, the deviatoric stress and energy at the final Hugoniot state are assumed to be $\sigma'_{11,2} = \eta\,\sigma'_{11,Y}$ and $\psi'_2 = \eta^2\psi'_Y$. Conservation of mass requires that

$$\frac{\lambda}{\lambda_{HEL}} = \frac{U_2 - u_{p,2}}{U_2 - u_{p,e}} \tag{1.11}$$

while the conservation of momentum can be written

$$\lambda_{HEL}V_0\left(\left|\sigma_{11,2}\right| - \left|\sigma_{11,HEL}\right|\right) = \left(U_2 - u_{p,e}\right)\left(u_{p,2} - u_{p,e}\right) \tag{1.12}$$

which, together, can be solved to obtain

$$u_{p,2} = u_{p,e} + \left(V_0(\lambda_{HEL} - \lambda)\left(\left|\sigma_{11,2}\right| - \left|\sigma_{11,HEL}\right|\right)\right)^{1/2} \tag{1.13}$$

And

$$U_2 = u_{p,e} + \lambda_{HEL}\left(V_0\frac{\left|\sigma_{11,2}\right| - \left|\sigma_{11,HEL}\right|}{\lambda_{HEL} - \lambda}\right)^{1/2}. \tag{1.14}$$

3.1.3 Comparison of Calculations of Single Crystal Hugoniot with Experimental Measurements

We computed the Hugoniot states for purely thermoelastic behavior of PETN in three orientations using the solution strategy described above. Figure 1 shows the resulting shock velocity versus particle velocity on the principal Hugoniot in comparison to measurements of single crystals with the corresponding orientations. The experimental data [21–23] are indicated by discrete points, i.e. square, triangle, and circle markers for (100), (110), and (001), respectively. The open markers indicate the measurements of Halleck and Wackerle [21], which correspond to the elastic precursor (rather than to a final Hugoniot state).

D. J. Luscher, M. J. Cawkwell, K. J. Ramos, R. L. Sandberg, C. A. Bolme
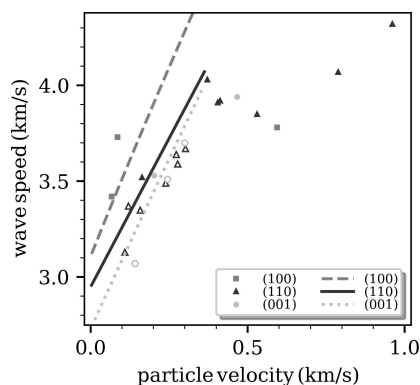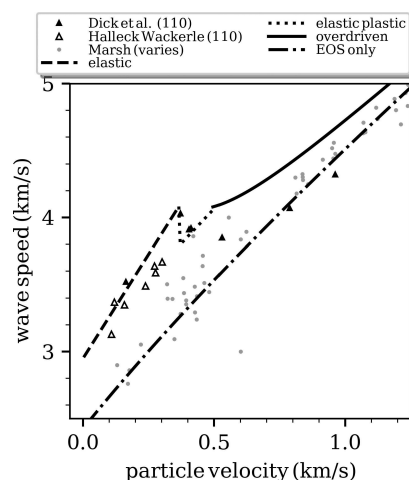

Figure 1. Wave speed versus particle velocity from several experiments [21–23] and our Hugoniot calculations using purely thermoelastic response for three different crystal orientations.

Figure 2. Wave speed versus particle velocity from several experiments [21–23,39] and our Hugoniot calculations for PETN (110) using a thermoelastic plus simple plasticity model. Triangle data points correspond to measurements for impacts on PETN (110).

The model exhibits trends that are consistent with those observed from the measurements. In particular, the ordering of the orientation dependence of the wave speeds is correct. The model also captures the slope for impacts on (110) and (001) reasonably well. The slope of the Hugoniot for impacts on (100) is only defined by two experimental points and does not match well, but the model does capture that this slope is higher than for impacts on (110) or (001).

The experiments depicted in Figure 1 did exhibit at least some amount of post-HEL inelastic deformation. However, the data points below 350 m/s correspond to the particle velocity at the HEL and the corresponding elastic precursor velocity. For impact velocities where our simple approach will exhibit purely elastic behavior, the experiments indicate some post-HEL inelastic response. However, based on these results it seems plausible that the effects of any inelastic deformation are small for impacts on single crystals resulting in particle velocities less than 350 m/s.

From these comparisons we estimate that an effective inviscid elastic limit for (110) impacts approximately corresponds to a compression ratio of $\lambda_{\text{HEL}} = 0.91$, which is associated with an axial stress of 2.7 GPa and a deviatoric component of 1.2 GPa in the model. These values generally agree with the measurements of Halleck and Wackerle [21], although their observation of a rate-dependent HEL and the more detailed viscous dislocation-based model they used to interpret these results are not accounted for here. Instead these values provide a simple estimate of the HEL that we subsequently used to perform calculations of the Hugoniot for impacts on (110) with the inclusion of inelastic effects. Deviation from elastic-to-inelastic and the corresponding path from the instantaneous-to-equilibrium Hugoniots can also vary depending on the density of defects and the nature of the deformation mechanisms. These were discussed in the seminal work on KCl and LiF [36–38].

Figure 2 compares the full Hugoniot solution including elastic and inelastic behavior from our simple model and the experimental measurements. The purely elastic solution is used for axial compressions that are below the approximate limit state and is indicated by a dashed line. The dotted line indicates the transition from purely elastic regime over which there is a two-wave structure. The solid line corresponds to the overdriven single elastic-inelastic wave case with the relaxation parameter $\eta = 1$. In addition, we plot the solution for the purely hydrostatic case using only the equation of state; this case would correspond to an overdriven single wave with inelastic behavior that entirely relaxes any non-hydrostatic stress, i.e. $\eta = 0$. The triangle markers indicate experimental measurements for (110) as in Figure 1, while the small gray circles correspond to the measurements tabulated in [39] for single crystals, but with unspecified orientations or specimen thickness. The model envelopes the measurements fairly well, although the measurements beyond 500 m/s seem to indicate more significant relaxation of non-hydrostatic stress than our upper bound estimate for the case $\eta = 1$.

3.2 Simple Model for Diffraction Peak Shifts

3.2.1 Summary of Previous experiments at LCLS

Bolme *et al.* [24] used the coherent, brilliant ultrafast, hard X-rays at the LCLS to investigate the collapse of a 10 µm diameter cylindrical void in PETN under the compression of a laser-driven shock. They utilized the intense femtosecond pulses from the LCLS to image the collapsing void using single-shot coherent X-ray diffractive imaging (CXDI). X-ray diffraction data was acquired using the LCLS X-ray beam on various regions of the specimens including near the void. These CXDI measurements and more detailed physics-

based modeling of the pore collapse are the subject of on-going research efforts that are not included in the present discussion.

One of the unique aspects of XFEL dynamic imaging is that the source is bright enough that simultaneous XRD can be fielded concurrently, enabling nanometer to micron scale imaging of material heterogeneity combined with atomic scale information of lattice deformation, the latter of which is used here for comparison with our simple model. Due to the characteristics of the X-ray beam, the Bragg condition for constructive interference is only satisfied for the (211)-reflection of the unshocked crystal, as shown in the integrated X-ray diffraction pattern in Figure 3. The target specimen geometry precluded simultaneous measurements of velocimetry during the shots for which X-ray diffraction data was collected. In order to characterize the shock strength associated with the laser drive, velocimetry was collected in a separate set of experiments employing the same laser drive set up directly into a LiF window and through a ~50 μm PETN crystal backed by a LiF window. Using these measurements and our simplified model for Hugoniot states under various assumptions, we estimate that the axial shock stress associated with the drive is on the order of 3.7–4.6 GPa.

Diffraction data similar to that shown in Figure 3 was collected for three similar shots with the same laser-drive configuration and same crystal orientation resulting in shifted diffraction peaks at $d = 3.25$, 3.30, and 3.30 Å. The timing of the X-ray strobe was selected to coincide with the incipient collapse of the void, thus these measurements probed a region that included both undeformed and deformed material, and some of the deformed region in the near vicinity of the pore would undoubtedly represent a departure from the simplistic assumptions of the present model. Nonetheless, the characteristic shift in the dominant peak provides an interesting data point to consider in the context of this simple model framework, even if only as a starting point for further investigations.
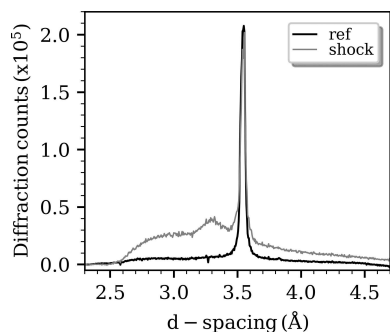
Figure 3. X-ray diffraction pattern from a PETN single crystal prior to (black) and (gray) during laser-driven shock compression experiment at LCLS [24]. The peak at $d = 3.56$ Å corresponding to the (211) plane is compressed behind the shock to approximately $d = 3.25$ Å.

3.2.2 A Model for the Observed Peak Shifts

Under conditions of shock loading along crystal directions that lead to pure longitudinal modes (which includes (110) in PETN), the total deformation gradient is simply $\mathbf{F} = \mathbf{Diag}(\lambda, 1, 1)$. However, the lattice deformation does not generally convect or flow with the total deformation and instead is described by the elastic deformation $\mathbf{F}_e$ in accordance with Equation (1.1). Due to the assumption that the inelastic deformation does not modify the crystal lattice (i.e. consistent with an isoclinic intermediate configuration typically adopted for crystal plasticity models) the deformed lattice unit cell vectors can be expressed as

$$\mathbf{a} = \mathbf{F}_e \cdot \mathbf{a}_0 \qquad \mathbf{b} = \mathbf{F}_e \cdot \mathbf{b}_0 \qquad \mathbf{c} = \mathbf{F}_e \cdot \mathbf{c}_0 \tag{1.15}$$

The reciprocal lattice (which is a basis for co-vectors) is related to the lattice vectors by

$$\mathbf{a}^* = \frac{\mathbf{b} \times \mathbf{c}}{\|\mathbf{a} \cdot (\mathbf{b} \times \mathbf{c})\|} \qquad \mathbf{b}^* = \frac{\mathbf{c} \times \mathbf{a}}{\|\mathbf{b} \cdot (\mathbf{c} \times \mathbf{a})\|}$$
$$\mathbf{c}^* = \frac{\mathbf{a} \times \mathbf{b}}{\|\mathbf{c} \cdot (\mathbf{a} \times \mathbf{b})\|} \tag{1.16}$$

The co-vector that is normal to and spans between two parallel crystallographic planes within the lattice is expressed simply by

$$\mathbf{r}_{(hkl)}{}^* = h\,\mathbf{a}^* + k\,\mathbf{b}^* + l\,\mathbf{c}^* \tag{1.17}$$

such that the interplanar spacing for crystallographic planes (hkl) within the deformed lattice can be computed as

$$d_{(hkl)} = \frac{1}{\left\|\mathbf{r}_{(hkl)}{}^*\right\|} \tag{1.18}$$

These well-known relationships of Equations (1.15) through (1.18) imply that we can learn something about the state of the elastic lattice deformation from shifts in the peak locations of measured diffraction spectra. Furthermore, through Eq. (1.1) we can possibly make inferences about the nature of inelastic deformation processes.

Purely elastic response can be represented by $\mathbf{F}_e = \mathbf{F} = \mathbf{Diag}(\lambda, 1, 1)$. The fully relaxed condition is approximated by the condition that the elastic part of the deformation is entirely volumetric, i.e. $\mathbf{F}_e = \lambda^{1/3}\mathbf{I}$. Finally, an approximation for the lattice deformation under a generally elastic-inelastic deformation is developed by considering that the total uniaxial deformation state was arrived at by a purely elastic deformation to the HEL, subsequently followed by isochoric inelastic deformation and purely volumetric elastic deformation. We can express this two-part process by the decomposition $\mathbf{F} = (\Delta\hat{\mathbf{F}})\mathbf{F}_{HEL}$ where $\Delta\hat{\mathbf{F}} = \hat{\mathbf{F}}_e\hat{\mathbf{F}}_{in}$ represents the generally elastic-inelastic deformation occur-

ring beyond the HEL. Because we assume $\hat{\mathbf{F}}_e$ is volumetric and $\mathbf{F}_{in}$ isochoric, the former can written as $\hat{\mathbf{F}}_e = (\lambda/\lambda_{HEL})^{1/3}\mathbf{I}$ such that the total elastic lattice deformation is obtained as $\mathbf{F}_e = (\lambda/\lambda_{HEL})^{1/3}\mathbf{Diag}(\lambda_{HEL}, 1, 1)$. Of course, this kinematic model makes restrictive assumptions about the evolution of deformation that are likely not satisfied by the actual deformation process, but it does provide a simple estimate for the lattice deformation that may result without a prior knowledge of the mechanisms that would accommodate the inelastic component of the deformation $\mathbf{F}_{in}$ such as plastic slip or fracture. This estimate assumes that the deformation causing non-hydrostatic stresses at the HEL is not relieved through the subsequent inelastic processes. A more accurate approach would be to employ a dynamic solution employing a physics-based model for the evolution of inelastic deformation.

Using these three separate assumptions about the inelastic deformation, i.e. none (elastic only), fully relaxed (volumetric only), relaxed beyond the HEL state (elastic-inelastic), in combination with the Hugoniot solution from above, we compute the resulting d-spacing for (211) planes as a function of shock stress, which is plotted in Figure 4. The light gray hatched region in Figure 4 indicates the estimated range of shock pressures for the LCLS experiments and the horizontal dark gray hatched region indicates the range of measured d-spacings. The purely volumetric estimate of the d-spacing underestimates the amount of lattice compression in that direction, while the elastic and elastic-inelastic estimates coincide with the measurements fairly well. The difference between the purely elastic and the elastic-inelastic estimates are negligible, which suggests that there is little sensitivity of the measured lattice geometry if the deviatoric stresses at the HEL cannot be further relaxed via inelastic mechanisms. On the other hand, there is a discernable difference for the purely relaxed (volumetric) esti-
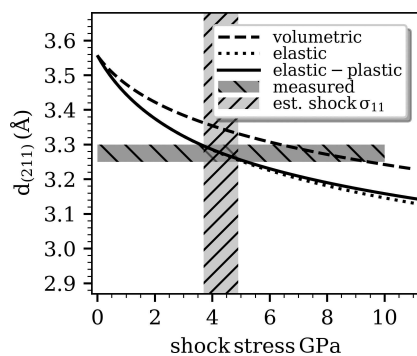
Figure 4. Estimated d-spacing for PETN (211) planes under shock compression to various stress levels assuming (dashed line) volumetric equation of state response only, (dotted line) purely elastic behavior without plastic flow, and (solid line) approximately elastic-perfectly plastic behavior. Light and dark gray hatched regions correspond to estimated shock stress and measured d-spacing range under shocked state, respectively.

mate. An interpretation of this result is that over the time and wave propagation distance scales of this experiment (10–20 ns and 40–80 µm, respectively) there is insufficient time to relax the non-hydrostatic stresses. Other experimental evidence exists to suggest that over larger time and wave propagation scales inelastic mechanisms further relax non-deviatoric stresses [21–23], thus a more detailed investigation including time-dependent plasticity and fracture mechanisms would provide more insight. These results reinforce the observation that significant deviatoric elastic lattice strains can be attained during the shock loading of PETN.

3.3 Large Elastic Strains

The results in the previous figures suggest that PETN experiences significant deviatoric elastic strains prior to and during the activation of inelastic deformation mechanisms. Consequently, one may expect that basing a model on different finite deformation strain measures would lead to different results. In many materials (e.g. metals), the deviatoric elastic strains are small, because they are limited by the ratio of material flow stress to the stiffness (i.e. $O(\varepsilon'_e) = O(\sigma_Y/G) < 0.01$). Consequently, the particular assumptions of finite deformation strain measures are typically not given much attention in theoretical descriptions and modeling of shock physics experiments. However, as elastic strains approach the order of a few percent, the stability of the material model must be considered.

3.3.1 Stability Conditions for Finite Deformation

Thermodynamic stability of an equation of state requires that the Gibbs free energy be concave in the pressure and temperature or that the Helmholtz free energy is convex in volume and concave in temperature. The generalization of this requirement to anisotropic finite elastic deformations is that the Helmholtz free energy is a polyconvex function of a basis set of the anisotropic invariants appropriate for the particular symmetry class and computed from the particular elastic strain (or deformation) tensor used. Polyconvexity of the Helmholtz free energy implies that the corresponding acoustic tensor is positive definite for all possible elastic deformations, and therefore, dynamic perturbations can be propagated through the deformed crystal at a finite wave speed. A mathematical expression of this requirement is

$$\delta\mathbf{F}_e : \frac{\rho_0\partial^2\psi(\mathbf{F}_e, T)}{\partial\mathbf{F}_e\partial\mathbf{F}_e} : \delta\mathbf{F}_e \geq 0 \quad \forall \mathbf{F}_e, \delta\mathbf{F}_e \quad \text{and} \quad T > 0 \quad (1.19)$$

Schroeder and Neff [40] have proposed a class of polyconvex functions suitable for transversely isotropic materials. This approach was extended to materials with cubic symmetry [41], however, the conditions of polyconvexity re-

strict the range of Zener anisotropy ratio $1/2 < A = 2\mathbb{C}_{44}/(\mathbb{C}_{11} - \mathbb{C}_{12}) < 1$. While many cubic metals do satisfy this constraint, the picture is a little less optimistic for energetic molecular crystals, which typically possess lower symmetry. Itskov and Aksel [42] expanded this treatment to develop a class of polyconvex free-energy functions which exhibit orthotropic symmetry. A general class of polyconvex functions for any crystal symmetry has been developed, but again, the conditions of polyconvexity and zero stress under zero deformation preclude arbitrary independent values of the stiffness coefficients for particular crystal symmetries [43]. We were unable to find any combination of terms in this class of functions that allow an exact match to the known elastic stiffness parameters for PETN (or RDX).

3.3.2 Euler Versus Lagrange Strains

Traditional models of thermoelasticity for single crystals make use of the Green-Lagrange strain, which is a nonlinear strain measure, within the St. Venant Kirchhoff expression for free energy. It is known that the St. Venant Kirchhoff free energy (quadratic in strain) is not polyconvex for arbitrarily large deformations [40,43,44]. In particular, there is a loss of stability under compression. Clayton [32] proposed an Eulerian strain measured (as used in Equation (1.2) for the above calculations) as an alternative to the Green-Lagrange strain and demonstrated that it provides a better representation of free-energy for the thermoelasticity of crystals under compression. However, the quadratic expression of free energy in terms of the Eulerian strain is also not polyconvex and fails under large deformations. However, a lack of polyconvexity does not imply that a particular form of the free energy function should be entirely avoided [44]. It is possible that the breakdown in mathematical stability for a particular expression occurs only under deformation cases where the material itself loses physical stability, e.g. at incipient lattice fracture, or that the potential is well-behaved under a significant range of deformation and unstable only under unexpected states of deformation.

To further demonstrate the implications of the finite deformation strain measure in the context of previous experiments, we consider the stresses resulting from the isothermal, uniaxial strain of a PETN single crystal separately using assumptions of Green-Lagrange and Euler strain measures in a quadratic expression of free-energy. In particular, for cases of Green-Lagrange strain we use

$$\mathbf{E} = \tfrac{1}{2}(\mathbf{F}_e^T \mathbf{F}_e - \mathbf{I})$$
$$\mathbf{S} = \mathbb{C} : \mathbf{E}$$
$$\boldsymbol{\sigma} = J_e^{-1} \mathbf{F}_e \mathbf{S} \mathbf{F}_e^T$$

(1.20)

and for the case of Euler strain we use

$$\boldsymbol{\varepsilon} = \tfrac{1}{2}(\mathbf{I} - \mathbf{F}_e^{-1} \mathbf{F}_e^{-T})\boldsymbol{\Sigma} = \mathbb{C} : \boldsymbol{\varepsilon}$$
$$\boldsymbol{\sigma} = J_e^{-1} \mathbf{F}_e^{-T} \boldsymbol{\Sigma} \mathbf{F}_e^{-1}$$

(1.21)

We consider cases of purely elastic, isothermal loading of PETN under uniaxial strain and under simple shear. The crystal is oriented such that the uniaxial compression is normal to (110) planes and the simple shearing is along the (110) planes, although results are similar for other orientations.

Uniaxial deformation: Figure 5 illustrates the differences in the variation in strain energy with axial stretch for the uniaxial strain case. While both strain measures produce nearly identical results at small strains (i.e. departures from $\lambda = 1$), they diverge at large strains and are generally non-symmetric with respect to tension and compression. The corresponding stresses are shown in Figure 6, which demonstrates that the Green-Lagrange strain measure leads to an instability under compression prior to reaching an axial
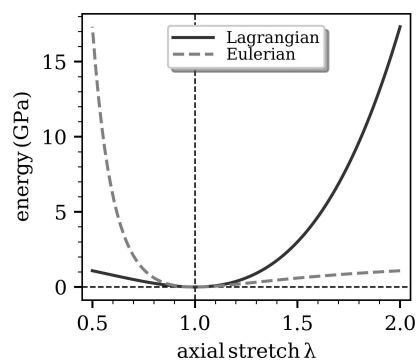
Figure 5. Variation of strain energy density for uniaxial deformation normal to (110) in PETN using Green-Lagrange (dark) and Euler (light dashed) strain measures.
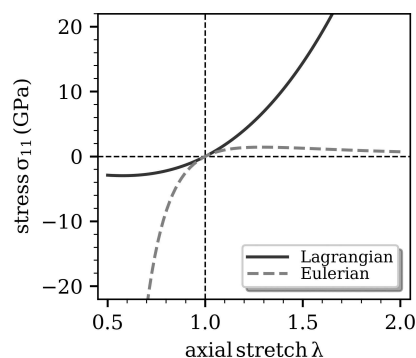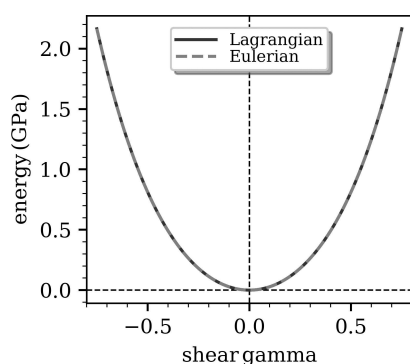
Figure 6. Variation of axial stress component for uniaxial deformation normal to (110) in PETN using Green-Lagrange (dark) and Euler (light dashed) strain measures. The model employing Green-Lagrange strain exhibits an instability prior to an axial compression of 4 GPa. The model employing Euler strain also exhibits an instability, but it is in the tensile region of deformation.

stress of 4 GPa. While these results do not include contributions from our nonlinear equation of state, which would help mitigate the instability, they do demonstrate the potential difficulty in using the Green-Lagrange strain in a quadratic free-energy expression for modeling shock compression. Some researchers have used higher-order expressions for the free-energy by employing third order elastic constants, which can also help mitigate this issue. On the other hand, the Euler strain is nicely behaved under compressions with the energy and stress increasing without bound as the volume is compressed toward zero. Using the Euler strain within the quadratic free energy expression moves the instability into the tension regime. It is plausible that this approach can be used with a brittle damage model to properly account for the inevitable fracture under tension.

Simple shear: Figures 7 and 8 demonstrate the behavior of models using Green-Lagrange and Euler strain measures under a case of simple shear loading. In this case the strain energy is identical throughout the deformation process (cf.

Figure 7. Variation of strain energy for simple shear on (110) in PETN using Green-Lagrange (dark) and Euler (light dashed) strain measures. The energy variations are identical, however the corresponding stresses are not.
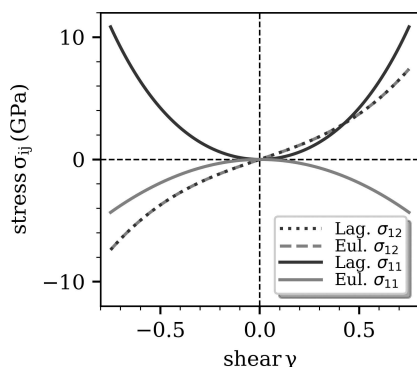
Figure 8. Variation of normal and shear stress components for simple shear on (110) in PETN using Green-Lagrange (dark) and Euler (light) strain measures. The shear stresses are identical, however the normal stress components are of opposite sense.

Figure 7), as is the shear stress (cf. Figure 8 dashed lines). However, the normal components of stress induced by the simple shearing deformation are of opposite sense; shearing induces a tensile normal stress using the Lagrange strain, but a compressive normal stress when using the Euler strain.

These results demonstrate that the particular strain measure adopted within the context of a general anisotropic thermoelastic-plastic model of single crystals likely deserves more attention for the case of PETN, and perhaps energetic molecular crystals more generally, because of the possibility of experiencing large elastic strains under shock compression.

4 Conclusions

In this paper we interpret previous experimental measurements of impacts on single crystal PETN in the context of a simple continuum model. Our approach enables an improved understanding of the deformation response of PETN without *a priori* knowledge of the detailed mechanisms that accommodate inelastic deformation. Hugoniot calculations using the simple model framework under various limiting assumptions envelope measured Hugoniot states reasonably well and suggest that non-negligible deviatoric elastic strains may exist in the shock compressed state for weak impacts.

An accompanying simple kinematic model for lattice deformation was used to estimate the expected shifts in X-ray diffraction peaks for the (211) plane under impacts normal to (110) planes. The results suggest that negligible relaxation of the deviatoric lattice deformation occurs on the short 10–20 ns time scale and 40–80 μm wave propagation distances of these experiments, and that the corresponding elastic strains may be large.

Because of the potentially large deviatoric elastic strains, the specific finite deformation strain measure used within thermomechanical single crystal models is of significant consequence. Our calculations demonstrate that the Green-Lagrange strain may be inappropriate for modeling the shock compression response of energetic molecular crystals and advocate for instead using the Eulerian strain measure [27]. Indeed, the Eulerian strain measure was also demonstrated to capture the orientation dependence of the Hugioniot well.

The work further demonstrates the utility of detailed measurements of the Hugoniot under weak impact conditions for constraining the assumptions of continuum models. Based on the calculated wave speed versus particle speed on the principal Hugoniot for separate assumptions of elastic, elastic-inelastic, and purely relaxed non-hydrostatic deformation, in comparison with the experimental measurements, it seems clear that some inelastic mechanism is triggered for impacts on (110) in PETN, especially above particle velocities above 500 m/s. This observation is

consistent with the previous interpretations of velocimetry from these experiments. For laser-driven shock loading of PETN along (110) over much shorter characteristic times, there appears to be negligible relaxation via inelastic deformation. Thus, the kinetics or viscosity of any relaxation mechanism is important to the overall response.

Acknowledgements

References

[1] F. P. Bowden, A. D. Yoffe, *Initiation and Growth of Explosion in Liquids and Solids*, Cambridge University Press **1952**.

[2] R. Menikoff, On beyond the standard model for high explosives: Challenges and obstacles to surmount, *AIP Conf. Proc.* **2009**, *1195*, 18.

[3] R. M. Doherty, D. S. Watt, Relationship between RDX properties and sensitivity, *Propellants, Explosives, and Pyrotechnics* **2008** *33*, 4.

[4] R. H. B. Bouma, A. G. Boluijt, H. J. Verbeek, A. E. D. M. van der Heijden, On the impact testing of cyclotrimethylene trinitramine with different internal qualities, *J. Appl. Phys.* **2008**, *103*, 093517.

[5] A. E. D. M. van der Heijden, R. H. B. Bouma, A. C. van der Steen, Physicochemical properties of nitramines influencing shock sensitivity, *Propellants Explos. Pyrotech.* **2004**, *29*, 304.

[6] H. Moulard, J. W. Kerry, A. Delcios, The effect of RDX particle size on the shock sensitivity of cast PBX formulations **1985**, *8th International Detonation Symposium*, 902.

[7] L. Borne, Influence of intragranular cavities of RDX particle batches on the sensitivity of cast wax bonded explosives, **1993** *10th International Detonation Symposium*, 286.

[8] K. J. Ramos, D. E. Hooks, D. F. Bahr, Direct observation of plasticity and quantitative hardness measurements in single crystal cyclotrimethylene trinitramine by nanoindentation, *Philos. Mag.* **2009**, *89*, 2381–2402.

[9] J. D. Clayton, R. Becker, Elastic-plastic behavior of cyclotrimethylene trinitramine single crystals under spherical indentation: Modeling and simulation, *J. Appl. Phys.* **2012**, *111*, 063512.

[10] H. G. Gallagher, J. C. Miller, D. B. Sheen, J. N. Sherwood, R. M. Vrcelj, Mechanical Properties of Beta-HMX, *Chemistry Central Journal* **2015**, *9*, 22.

[11] M. J. Cawkwell, D. S. Montgomery, K. J. Ramos, C. A. Bolme, Free energy based equation of state for pentaerythritol tetranitrate, *J. Phys. Chem. A* **2016**, *121*, 238–243.

[12] D. E. Hooks, K. J. Ramos, C. A. Bolme, M. J. Cawkwell, Elasticity of Crystalline Explosives, *Propellants, Explosives and Pyrotechnics* **2015**, *40*, 333.

[13] T. D. Sewell, C. M. Bennett, Monte Carlo Calculations of the elastic moduli and pressure-volume-temperature equation of state for hexahydro-1,3,5-trinitro-1,3,5-triazine, *J. Appl. Phys.* **2000**, *88*, 88.

[14] M. J. Cawkwell, D. J. Luscher, F. L. Addessio, K. J. Ramos, Equations of State for the alpha and gamma polymorphs of cyclotrimethylene trinitramine, *J. Appl. Phys.* **2016**, *119*, 185106.

[15] R. Menikoff, J. J. Dick, D. E. Hooks, Analysis of wave profiles in cyclotetramethylene tetranitramine, *J. Appl. Phys.* **2005**, *97*, 023529.

[16] D. J. Luscher, F. L. Addessio, M. J. Cawkwell, K. J. Ramos, A dislocation density-based continuum model of the anisotropic shock response of single crystal α-cyclotrimethylene trinitramine, *J. Mech. Phys. Solids* **2017**, *98*, 63–86.

[17] F. L. Addessio, D. J. Luscher, M. J. Cawkwell, K. J. Ramos, A single crystal model for the high rate deformation of cyclotrimethylene trinitramine including phase transformations and slip, *J. Appl. Phys.* **2017**, *121*, 185902.

[18] N. R. Barton, N. W. Winter, J. E. Reaugh, Defect evolution and pore collapse in crystalline energetic materials, *Modell. Simul. Mater. Sci. Eng.* **2009**, *17*, 035003.

[19] R. A. Austin, N. R. Barton, J. E. Reaugh, L. E. Fried, Direct numerical simulation of shear localization and decomposition reactions in shock-loaded HMX crystal, *J. Appl. Phys.* **2015**, *117*, 185902.

[20] J. W. Conant, H. H. Cady, R. R. Ryan, J. L. Yarnell, J. M. Newsam, The Atom Positions of Pentaerythritol Tetranitrate (PETN, C5H8 N4O12) Determined by X-ray and by Neutron Diffraction **1979**, *Los Alamos National Laboratory Report*, LA-7756-MS.

[21] P. M. Halleck, J. Wackerle, Dynamic elastic-plastic properties of single crystal pentaerythritol tetranitrate, *J. Appl. Phys.* **1976**, *47*, 976–982.

[22] J. J. Dick, J. P. Ritchie, Molecular mechanics modeling of shear and the crystal orientation dependence of the elastic precursor shock strength in pentaerythritol tetranitrate, *J. Appl. Phys.* **1994**, *76*, 2726–2737.

[23] J. J. Dick, Anomalous shock initiation of detonation in pentaerythritol tetranitrate crystals, *J. Appl. Phys.* **1997**, *81*, 601–612.

[24] C. A. Bolme, K. J. Ramos, R. L. Sandberg, E. Watkins, S. McGrane, M. J. Cawkwell, D. S. Moore, Dynamic Evolution of High Explosives (HE): A Summary of Recent Physics Insights for Next-Generation Models Obtained at 3rd and 4th-Generation Light Sources **2018**, *Los Alamos National Laboratory Technical Report*, LA-UR-18-28777.

[25] H. G. Gallagher, P. J. Halfpenny, J. Miller, J. N. Sherwood, Dislocation slip systems in pentaerythritol tetranitrate (PETN) and cyclotrimethylene trinitramine (RDX), *Philos. T. R. Soc. A* **1992**, *339*, 293–303.

[26] R. M. Eaton, T. D. Sewell, Shock-induced inelastic deformation in oriented crystalline pentaerythritol tetranitrate, *J. Phys. Chem. C* **2012**, *116*, 2226.

[27] M. J. Cawkwell, N. Mohan, D. J. Luscher, K. J. Ramos, Dissociation of (111) dislocations on {1–10} in pentaerythritol tetranitrate, *Philos. Mag.* **2019**, *99*, 1079–1089.

[28] J. J. Dick, Effect of crystal orientation on shock initiation sensitivity of pentaerythritol tetranitrate explosive, *Appl. Phys. Lett.* **1984**, *44*, 859–861.

[29] J. M. Winey, Y. M. Gupta, Anisotropic material model and wave propagation simulations for shocked pentaerythritol tetranitrate single crystals, *J. Appl. Phys.* **2010**, *107*, 103505.

[30] Y. Cai, F. P. Zhao, Q. An, H. A. Wu, W. A. Goddard III, S. N. Luo, Shock response of single crystal and nanocrystalline pentaerythritol tetranitrate: Implications to hotspot formation in energetic materials, *J. Chem. Phys.* **2013**, *139*, 164704.

D. J. Luscher, M. J. Cawkwell, K. J. Ramos, R. L. Sandberg, C. A. Bolme

[31] P. J. Halfpenny, K. J. Roberts, J. N. Sherwood, Dislocations in Energetic Materials. 2. Characterization of the Growth-Induced Dislocation Structure of Pentaerythritol Tetranitrate (PETN), *J. Appl. Crystallogr.* **1984**, *17*, 320.

[32] J. D. Clayton, Nonlinear Eulerian thermoelasticity for anisotropic crystals, *J. Mech. Phys. Solids* **2013**, *61*, 1983–2014.

[33] H. S. Udaykumar, L. Tran, D. M. Belk, K. J. Vanden, An Eulerian method for computation of multimaterial impact with ENO shock-capturing and sharp interfaces, *J. Comput. Phys.* **2003**, *186*, 136–177.

[34] E. J. Lieberman, X. Liu, N. R. Morgan, D. J. Luscher, D. E. Burton, A higher-order Lagrangian discontinuous Galerkin hydrodynamic method for solid dynamics, *Comput. Methods in Appl. Mech. Eng.* **2019**, *353*, 467–490.

[35] B. Sun, J. M. Winey, N. Hemmi, Z. A. Dreger, K. A. Zimmerman, Y. M. Gupta, D. H. Torchinsky, K. A. Nelson, Second-order elastic constants of pentaerythritol tetranitrate and cyclotrimethylene trinitramine using impulsive stimulated thermal scattering, *J. Appl. Phys.* **2008**, *104*, 073517.

[36] D. B. Hayes, Polymorphic phase transformation rates in shock-loaded potassium chloride, *J. Appl. Phys.*, **1974**, *45*, 1208

[37] J. R. Asay, Y. M. Gupta, Effect of Impurity Clustering on Elastic Precursor Decay in LiF, *J. Appl. Phys.* **1972**, *43*, 2220

[38] B. J. Jensen, Y. M. Gupta, Time-resolved x-ray diffraction experiments to examine the elastic plastic transition in shocked magnesium doped LiF, *J. Appl. Phys.* **2008**, *104*, 013510.

[39] S. P. Marsh, LASL shock Hugoniot data (Vol. 5) **1980**. Univ of California Press.

[40] J. Schröder, P. Neff, Invariant formulation of hyperelastic transverse isotropy based on polyconvex free energy functions, *Int. J. Solids Struct.* **2003**, *40*, 401–445.

[41] N. Kambouchev, J. Fernandez, R. Radovitzky, 2007. A polyconvex model for materials with cubic symmetry, *Modell. Simul. Mater. Sci. Eng.* **2007**, *15*, 451–467.

[42] M. Itskov, N. Aksel, A class of orthotropic and transversely isotropic hyperelastic constitutive models based on a polyconvex strain energy function, *Int. J. Solids Struct.* **2004**, *41*, 3833–3848.

[43] J. Schröder, P. Neff, V. Ebbing, Anisotropic polyconvex energies on the basis of crystallographic motivated structural tensors, *J. Mech. Phys. Solids* **2008**, *56*, 3486–3506.

[44] S. Hartmann, P. Neff, Polyconvexity of generalized polynomial-type hyperelastic strain energy functions for near-incompressibility, *Int. J. Solids Struct.* **2003**, *40*, 2767–2791.